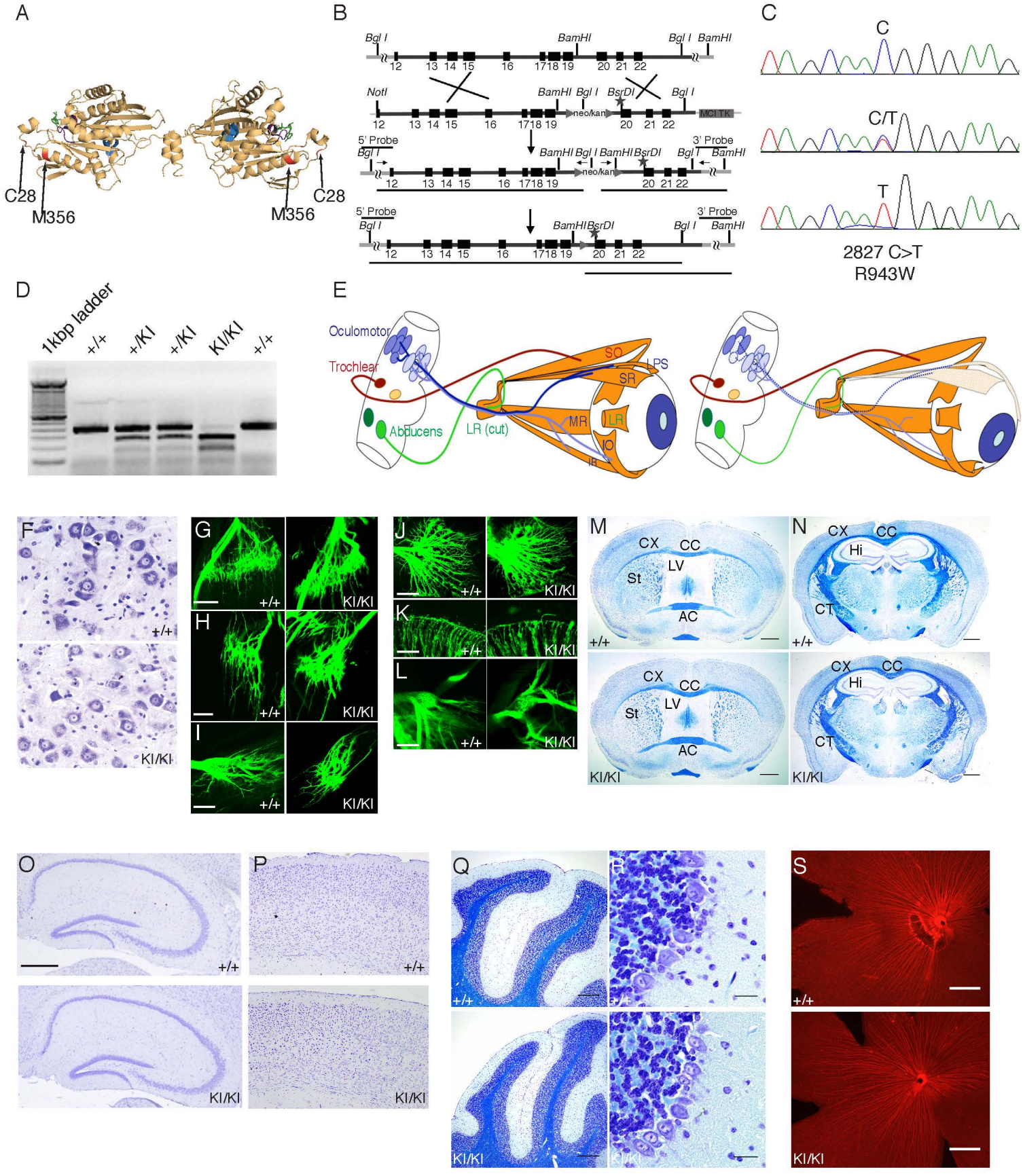
A
C28
M356
C28
M356
B
Bgl I
BamHI
Bgl I
BamHI
12 13 14 15 16 1718 19 20 21 22
NotI
BamHI
Bgl I
BsrDI
Bgl I
neo/kan
MCI TK
5' Probe
3' Probe
BamHI Bgl I BamHI BsrDI Bgl I BamHI
BamHI BsrDI
C
C
C/T
T
2827 C>T
R943W
D
1kbp ladder
+/+
+/KI
+/KI
KI/KI
+/+
E
Oculomotor
Trochlear
Abducens
LR (cut)
SO
LPS
SR
MR
LR
IO
IR
F
G
H
I
J
K
L
M
CX
CC
LV
St
AC
N
CX
CC
Hi
CT
+/+
KI/KI
O
P
Q
R
S

Figure S1

Figure S1: Generation and analysis of the Kif21a R954W knock-in (KI) mouse model. Related to Figure 1.

(A) The crystal structure of dimeric motor-neck domains of Drosophila Kif5a (Protein Data Bank [PDB] code 2Y5W), onto which we mapped and highlighted in red the residues corresponding the C28 and M356 (arrows) in human KIF21A (1-1674) (NCBI accession No. NM_001173464.1, NP_001166935) by using PyMOL software (1.1r1, http://www.pymol.org/) based on the amino acid sequences alignment and homology. Blue, purple, and green highlight the microtubule binding site, ATP binding site, and ADP-Mg^{2+}, respectively. **(B)** Targeting scheme used to generate the *Kif21a*$^{KI/KI}$ mice includes the endogenous 11.2 kb locus containing exons 12-22 of Kif21a (top), the targeting construct (2nd row), the endogenous locus following homologous recombination (3rd row) and following removal of the neo cassette (bottom). Restriction enzyme sites are named and the location of the Southern probes indicated. Locations of the exon 20 2,827C→T missense mutation (starred), the neo cassette (grey box), and the loxp sites (triangles) within the targeting construct are indicated. **(C)** Sequence analysis of genomic DNA confirms WT alleles in *Kif21a*$^{+/+}$ (top), a heterozygous 2,827C→T mutation in *Kif21a*$^{KI/+}$ (middle), and a homozygous 2,827C→T mutation in *Kif21a*$^{KI/KI}$ (bottom) mice. **(D)** RFLP analysis of genomic PCR products that contained the 2,827C→T mutation. The mutation created a new BsrD I site resulting in a unique banding pattern for each genotype following PCR product digestion with BsrD I. **(E)** Schematic of the anatomy of the human oculomotor axis with nuclei and nerves innervating the extraocular muscles controlling the right eyeball in normal (left) and CFEOM1 disease state (right). In each schematic, the brainstem is translucent, and the paired right (lighter fill) and left (darker fill) ocular cranial nuclei are shown. The abducens nuclei are light and dark green, and the abducens nerve that innervates the lateral rectus muscle (LR, cut) within the right orbit arises from motor neurons in the ipsilateral right abducens nucleus and exits the pons ventrally (light green nerve). The trochlear nuclei are light and dark brown, and the trochlear nerve that innervates the superior oblique muscle (SO) within the right orbit arises from motor neurons in the contralateral dark-brown left trochlear nucleus and exits the midbrain dorsally (dark brown nerve). The oculomotor nuclei are light and dark blue, and each is made up of five subnuclei. The motor axons of the subnuclei destined to innervate the right medial rectus (MR), inferior rectus (IR), and inferior oblique (IO) muscles arise from motor neurons in the right ipsilateral light blue oculomotor nucleus and exit the brainstem ventrally to form the inferior division of the oculomotor nerve (light blue nerve). The motor axons of the subnuclei destined to innervate the right levator palpebrae superioris (LPS) and superior rectus (SR) muscles arise from motor neurons in the left contralateral dark blue oculomotor nucleus and cross the midline, pass through the right oculomotor nucleus, and join the oculomotor nerve as its superior (dark blue nerve). In the disease state (right), postmortem examination of an individual with CFEOM1 resulting from the R954W substitution revealed absence of the contralateral LPS and SR motor neurons (dotted dark blue subnuclei), absence of the superior division of the oculomotor nerve (dotted dark blue superior division), and hypoplasia of the LSP and SR muscles (dotted muscles). The abducens nerve was also thin (note thinner light green nerve) (Engle et al., 1997). (F) Representative images of Nissl staining of motor neurons in an adult *Kif21a*$^{+/+}$ (top) and *Kif21a*$^{KI/KI}$ (bottom) oculomotor nucleus used for cell counts in Figure 1G (n=4, 4). To avoid double counting, only the neurons with a visible nucleolus were counted within a given section. **(G-I)** Following anterograde dye tracing and isolation of EOMs, the IR (G), SO (H), and MR (I) muscles had qualitatively normal innervation in *Kif21a*$^{KI/KI}$ compared to WT mice. Scale bars 30 µm. **(J-L)** Following anterograde dye tracing, the nasal pad (J), cochlea (K), and ciliary ganglion (L) had normal sensory efferent innervation in *Kif21a*$^{KI/KI}$ compared to WT mice. Scale bars 20 µm. **(M and N)** Luxol fast blue stain for myelin with Nissl counterstain of coronal sections of adult *Kif21a*$^{+/+}$ and *Kif21a*$^{KI/KI}$ brains at the level of the anterior commissure (M) and

hippocampus (N) reveal no detectable abnormalities in architecture of corpus callosum (CC), anterior commissure (AC), cortex (CX), striatum (St), hippocampus (Hi), corticospinal tract (CT), and lateral ventricle (LV) in the mutant brain compared to WT (n=5, 5). Of note, the slight difference in the appearance of the WT and mutant habenular nuclei in (N) results from slight differences in orientation. **(O and P)** Higher power examination of Nissl stained serial sections of the hippocampus (O) and cortex (P) showed no detectable architectural abnormalities in adult *Kif21a*$^{+/+}$ and *Kif21a*$^{KI/KI}$ brains (n=6, 5)**.** **(Q and R)** Luxol fast blue stain for myelin with Nissl counterstain of sagittal sections of the cerebellum of adult *Kif21a*$^{+/+}$ and *Kif21a*$^{KI/KI}$ showed no detectable abnormalities in architecture (n=3, 3). **(S)** Flat-mount retina immunofluorescent staining with anti-neurofilament antibody showed no detectable abnormalities in retinal ganglion cell axonal projections in adult *Kif21a*$^{KI/KI}$ mice compared to *Kif21a*$^{+/+}$ mice (n=7, 5). Scale bars 400 μm (M, N), 500 μm (O), 200 μm (P), 100 μm (Q and S), 20 μm (R).

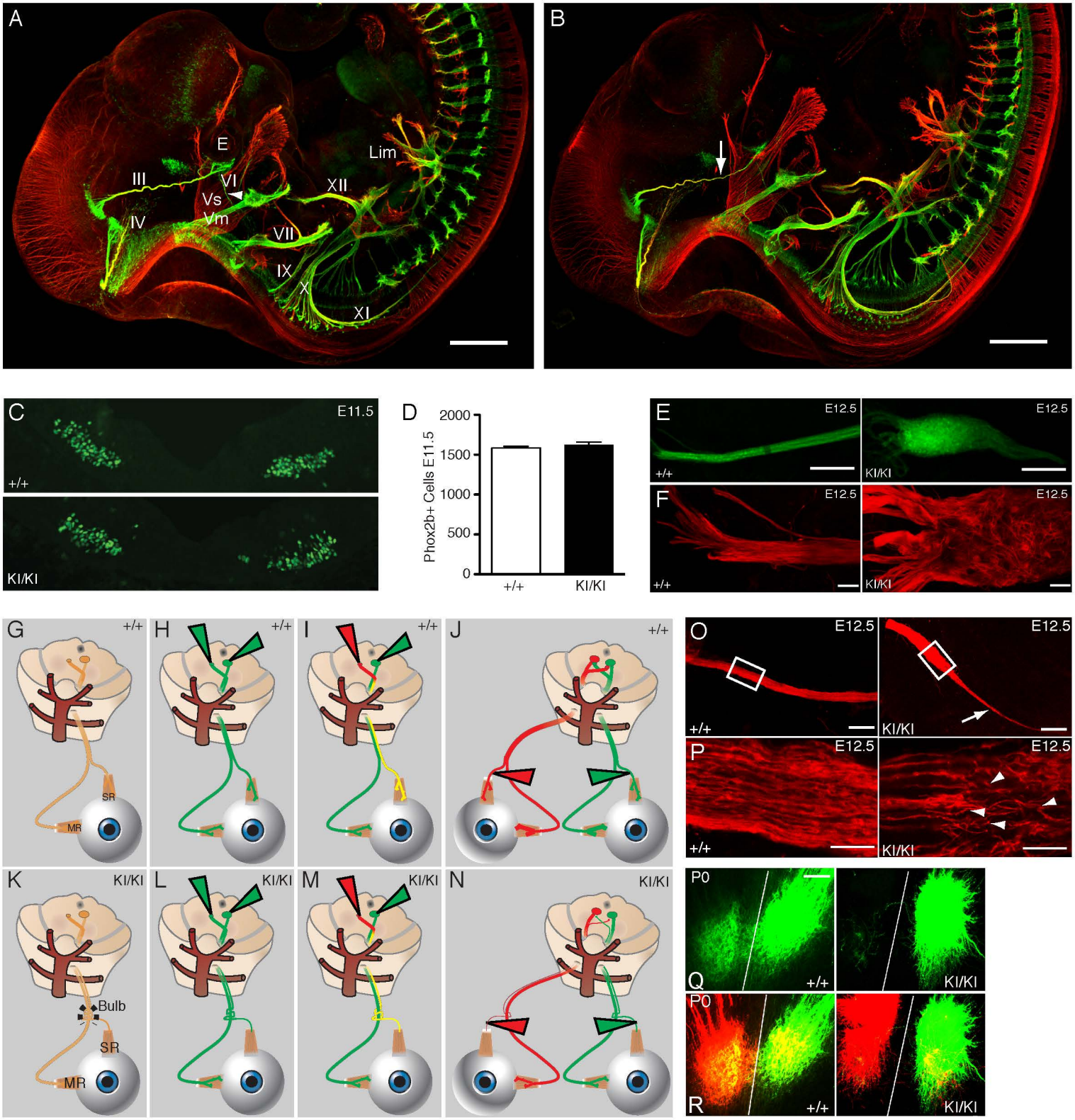
A
E
III
VI
Vs
Vm
IV
VII
IX
X
XI
XII
Lim
B
C
E11.5
+/+
KI/KI
D
Phox2b+ Cells E11.5
2000
1500
1000
500
0
+/+
KI/KI
E
E12.5
+/+
KI/KI
F
E12.5
+/+
KI/KI
G
+/+
SR
MR
H
+/+
I
+/+
J
+/+
K
KI/KI
Bulb
SR
MR
L
KI/KI
M
KI/KI
N
KI/KI
O
E12.5
+/+
KI/KI
P
E12.5
+/+
KI/KI
P0
Q
+/+
KI/KI
P0
R
+/+
KI/KI

Figure S2

Figure S2: Oculomotor nerve pathology in *Kif21a*$^{KI/KI}$ mice. Related to Figure 2 and Supplemental Movies S1 and S2.

(A, B) Whole mount fluorescent immunostaining with anti-neurofilament (red) and anti-GFP (green) antibodies of E11.5 *Kif21a*$^{+/+}$*;Isl*^{MN}*:GFP* (A) and *Kif21a*$^{KI/KI}$ *;Isl*^{MN}*:GFP* (B) embryos (n=22, 20) reveal similar trajectories of the WT and mutant cranial and spinal nerves. Differences in red versus green intensity of limb and spinal nerves between embryos simply reflects differences in color balance. Arrowhead in (A) points to abducens nerve (VI); Arrow in (B) highlights the distal thinning of mutant oculomotor nerve compared to WT nerve. Scale bars 500 μm. Higher magnification of the cranial nerves of these embryos are presented in Figure 2A and 2B. **(C)** Representative images of coronal sections through the oculomotor nuclei of E11.5 *Kif21a*$^{+/+}$ (top) and *Kif21a*$^{KI/KI}$ (bottom) embryos labeled with *Phox2b*. **(D)** Quantification of the number of *Phox2b*-labeled neurons in bilateral oculomotor nuclei at E11.5 in (B, C) revealed equal numbers of neurons in *Kif21a*$^{+/+}$ and *Kif21a*$^{KI/KI}$ embryos (n=3, 3; 1584±20 vs. 1623± 40, p=0.39). **(E)** Confocal images of proximal oculomotor nerves extending from brainstem toward the orbit (left to right of each image) from E12.5 *Kif21a*$^{+/+}$*;Isl*^{MN}*:GFP* WT (left) and *Kif21a*$^{KI/KI}$*;Isl*^{MN}*:GFP* mutant (right) embryos. Scale bar 100 μm. **(F)** Confocal images of WT (left) and mutant (right) oculomotor nerves from (A) stained with anti-neurofilament antibody. Scale bars 20 μm. In both E and F, note the bulb-like structure formed within the proximal nerve immediately following fasciculation of the nerve roots that have exited the brainstem in the mutant (right) and not WT (left) nerve. **(G-N)** Schematic diagrams of oculomotor anatomy and lipophilic dye injection paradigms in WT (G-J) and mutant (K-N) mice. The midbrain is depicted with the superior (contralateral) and inferior (ipsilateral) oculomotor axons exiting the midbrain and innervating the superior rectus muscle and medial rectus muscle, respectively. Vessels surrounding the midbrain are depicted in dark brown. Dye placement and color is represented by a green or red triangle. (G, K) Schematic of uninjected WT and mutant anatomy. (H, L) Schematic of one-color anterograde labeling (green) reveals reduced innervation of superior division muscles in *Kif21a*$^{KI/KI}$ embryos; primary data in Figures 1L-Q, S1G-L. (I, M) Schematic of two-color anterograde labeling (green and red) reveals premature termination within the bulb of primarily yellow superior division axons in *Kif21a*$^{KI/KI}$ embryos; primary data in Figure 2O-T. (J, N) Schematic of one and two color retrograde labeling of inferior ipsilateral and superior contralateral axons and motor neurons reveals reduction in filling of contralateral superior division axons and motor neurons following dye placement in the orbit in *Kif21a*$^{KI/KI}$ embryos; primary single-color data in Figure 2AA-AF and two-color data in Figure S2Q-R. **(O, P)** Confocal images of whole oculomotor nerve preparations after placing dye-soaked filter strips in the ventral midbrain at E12.5 confirmed results in Figure 2I-2N, revealing the bulb with distal thinning in *Kif21a*$^{KI/KI}$ (O, right, arrow) and not *Kif21a*$^{+/+}$ (O, left) embryos. Moreover, single confocal optical slices at higher magnification of boxed regions of the *Kif21a*$^{KI/KI}$ (P, right) and not *Kif21a*$^{+/+}$ (P, left) nerves revealed misdirected and stalled oculomotor axons (P, arrowheads) that wandered inappropriately, a subset of which appeared to prematurely terminate within the bulb (n=4, 5). **(Q, R)** Vibratome sections (100 μm in thickness) from P0 *Kif21a*$^{+/+}$ (left) and *Kif21a*$^{KI/KI}$ (right) midbrains after red and green lipophilic dye placement in right and left orbit, respectively, and retrograde labeling of the oculomotor nuclei. White lines indicate midline. The motor neurons of the oculomotor superior division that were successfully labeled from the contralateral orbit appear yellow, and are reduced in *Kif21a*$^{KI/KI}$ compared to *Kif21a*$^{+/+}$ mice (n=3, 3). Scale bar 30 μm. Abbreviations: SR = superior rectus, MR = medial rectus, III=oculomotor nerve, IV=trochlear nerve, Vs=sensory branches of the trigeminal nerve, Vm=motor branch of the trigeminal nerve, VI=abducens nerve, VII=facial nerve, IX=glossopharyngeal nerve, XI=accessory nerve, XII=hypoglossal nerve, E=eye.

A

cross-sectional area of nerve (μm2)				
WT/WT-proximal #1/#2	WT/WT-distal #1/#2	KI/KI-proximal #3/#4	KI/KI-distal #3/#4	KI/KI-bulb #3/#4
877 / 566	797 / 624	985 / 981	315 / 322	3171 / 3942

B

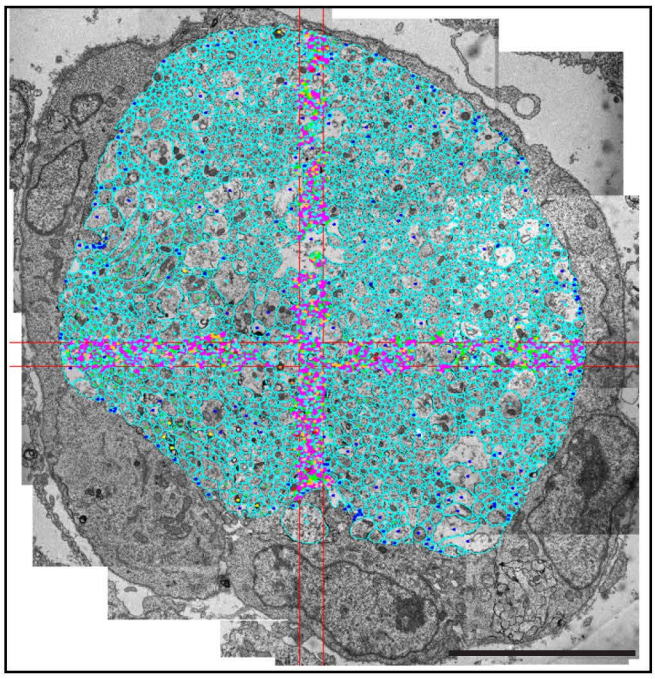

C

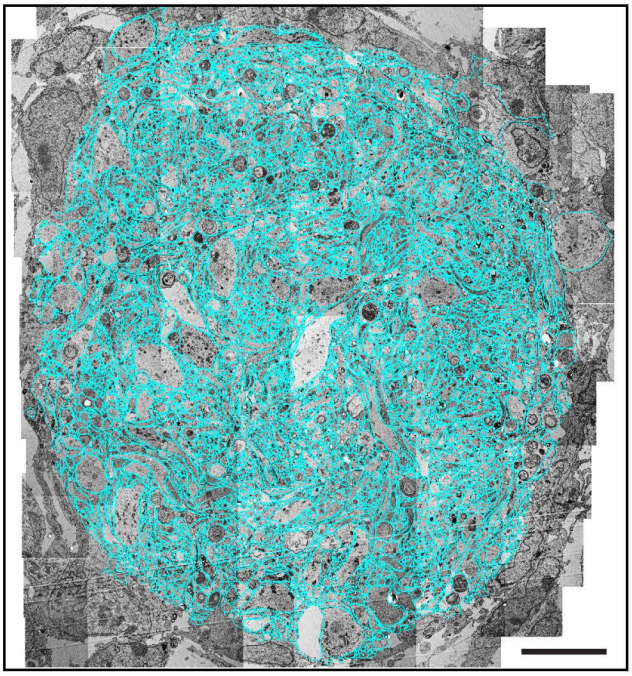

D

number					
	cross-sectional axon	longitudinal axon	central growth cone	lamellipodia/filopodia	degenerating axon
WT/WT-proximal #1/#2	2475 / 2351	12 / 23	128 / 129	125 / 215	8 / 12
WT/WT-distal #1/#2	2488 / 2311	4 / 15	73 / 219	97 / 191	5 / 32
KI/KI-proximal #3/#4	1976 / 1931	34 / 17	90 / 140	162 / 298	24 / 39
KI/KI-distal #3/#4	863 / 865	14 / 4	27 / 30	97 / 203	18 / 5
KI/KI-bulb #3/#4	2515 / 1795	283/ 404	465 / 482	920 / 2780	72 / 227

E

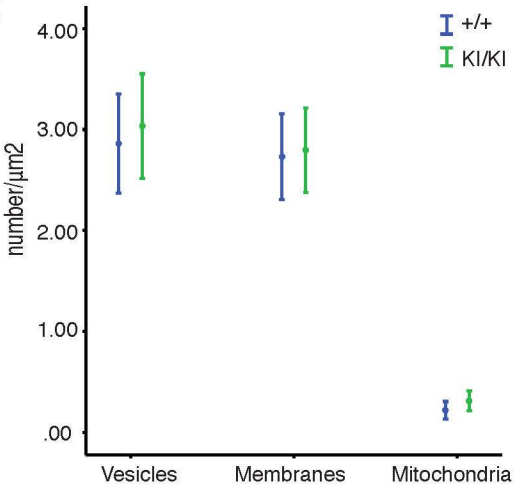

F

Density (number/μm2) (mean±SEM)			
	vesicle	membrane	mitochondria
WT/WT-proximal	2.86±0.2	2.73±0.2	0.22±0.04
KI/KI-proximal	3.03±0.3	2.80±0.2	0.31±0.05

G

average area (μm2/number)					
	cross-sectional axon	longitudinal axon	central growth cone	lamellipodia/filopodia	degenerating axon
WT/WT-proximal #1/#2	0.21 / 0.13	0.45 / 0.28	1.12 / 0.80	0.82 / 0.35	0.60 / 0.39
WT/WT-distal #1/#2	0.17 / 0.14	0.33 / 0.40	1.02 / 0.75	1.18 / 0.25	0.66 / 0.33
KI/KI-proximal #3/#4	0.35 / 0.32	1.22 / 0.90	1.09 / 0.90	0.45 / 0.24	0.74 / 0.80
KI/KI-distal #3/#4	0.23 / 0.23	0.91 / 0.25	1.08 / 0.89	0.29 / 0.22	0.32 / 0.53
KI/KI-bulb #3/#4	0.44 / 0.42	1.61 / 1.14	1.62 / 2.07	0.40 / 0.25	1.55 / 1.72

Figure S3

Figure S3: Ultrastructural analysis of E12.5 *Kif21a*$^{KI/KI}$ versus *Kif21a*$^{+/+}$ oculomotor nerves. Related to Figure 4.

(A) Measurements of cross-sectional areas of E12.5 oculomotor nerves in *Kif21a*$^{+/+}$*;Isl*^{MN}*:GFP* and *Kif21a*$^{KI/KI}$*;Isl*^{MN}*:GFP* mice within each of the EM sections. **(B, C)** Stitched 4800x electron microscopy (EM) cross-sectional images through a proximal WT oculomotor nerve (B) and the bulb of a mutant oculomotor nerve (C). The circumference of each object within each oculomotor nerve was traced by hand using Fiji. Scale bars 10 μm; note difference in enlargements between B and C. **(D)** Tabulation of numbers of cross-sectional axons, longitudinal axons, central growth cones, lamellipodia/filopodia, and degenerating axons within each nerve cross-section. **(E, F)** A grid was placed over the four proximal nerve cross-sections as demonstrated by the pink lines in (B), and the average densities of vesicles, membranes, and mitochondria in all axons located within the grid space were calculated and are presented in graph (E) and table (F) format. Values are represented as mean ± SEM. **(G)** Table of the average area of identified objects in (D). Abbreviations: #1 and #2 denote WT nerves, #3 and #4 denote mutant nerves. p=proximal cross-section, d=distal cross-section, b=bulb cross-section.

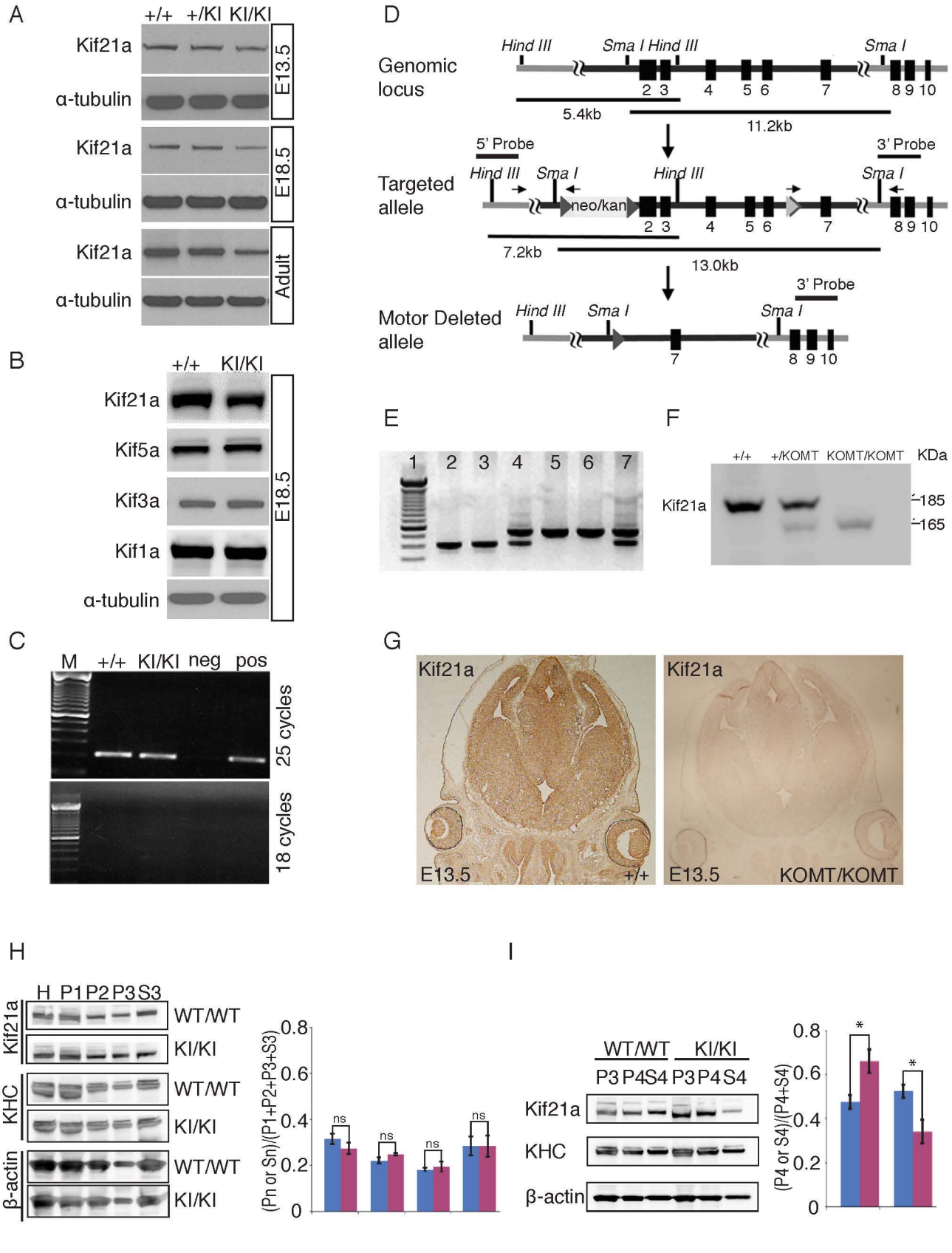
A
+/+ +/KI KI/KI
Kif21a
α-tubulin
E13.5
Kif21a
α-tubulin
E18.5
Kif21a
α-tubulin
Adult
B
+/+ KI/KI
Kif21a
Kif5a
Kif3a
Kif1a
α-tubulin
E18.5
C
M +/+ KI/KI neg pos
25 cycles
18 cycles
D
Genomic locus
Hind III
Sma I Hind III
Sma I
2 3 4 5 6 7 8 9 10
5.4kb
11.2kb
5' Probe
3' Probe
Targeted allele
Hind III Sma I
neo/kan
Hind III
Sma I
2 3 4 5 6 7 8 9 10
7.2kb
13.0kb
3' Probe
Motor Deleted allele
Hind III Sma I
Sma I
7
8 9 10
E
1 2 3 4 5 6 7
F
+/+ +/KOMT KOMT/KOMT KDa
Kif21a
185
165
G
Kif21a
E13.5 +/+
Kif21a
E13.5 KOMT/KOMT
H
H P1 P2 P3 S3
Kif21a
KHC
β-actin
WT/WT
KI/KI
WT/WT
KI/KI
WT/WT
KI/KI
(Pn or Sn)/(P1+P2+P3+S3)
0.8
0.6
0.4
0.2
0
ns
I
WT/WT KI/KI
P3 P4 S4 P3 P4 S4
Kif21a
KHC
β-actin
(P4 or S4)/(P4+S4)
0.8
0.6
0.4
0.2
0
*
*

Figure S4

Figure S4: Generation of Kif21a knock-out motor truncated *Kif21a*$^{KOMT/KOMT}$ mice. Related to Figure 5.

(A) Representative western blot (n=3) of E13.5, E18.5, and adult brain lysates from *Kif21a*$^{+/+}$, *Kif21a*$^{+/KI}$ and *Kif21a*$^{KI/KI}$ mice. Kif21a protein levels decreased most notably in brain lysates from adult *Kif21a*$^{KI/KI}$ mice. **(B)** Representative western blot (n=3) of E18.5 brain lysates from *Kif21a*$^{+/+}$ and *Kif21a*$^{KI/KI}$ mice revealed reduced level of Kif21a protein consistent with (A), with no change in levels of other kinesin motor proteins examined. **(C)** 18 and 25 cycle semi-quantitative real time PCR of total brain mRNA from E18.5 *Kif21a*$^{KI/KI}$ and *Kif21a*$^{+/+}$ mice (n=3). **(D)** Targeting scheme for *Kif21a*$^{KOMT/KOMT}$ mice depicting the endogenous 11kb locus containing exons 2-7 of Kif21a, the targeting vector with location of loxp sites, and final targeted locus. **(E)** Kif21a^{KOMT} genotyping: 652 base pair (bp) PCR product is generated by PCR from the WT allele, and 399 bp product from the mutant allele. **(F)** Western blot analysis of Kif21a protein using an antibody to its extreme C-terminus (Tischfield et al., 2010) detected a truncated motorless species in *Kif21a*$^{KOMT/KOMT}$ brain lysates at a level of ~15% of WT. Heterozygous mice expressed both WT and truncated Kif21a protein. **(G)** Immunohistochemistry with Kif21a antibody on sections from E13.5 *Kif21a*$^{+/+}$ and *Kif21a*$^{KOMT/KOMT}$ embryos. No specific signal was detected in brain sections from *Kif21a*$^{KOMT/KOMT}$ compared to *Kif21a*$^{+/+}$ embryos. **(H)** Representative western blot showing the presence of Kif21a in P1, P2, P3, and S3 cellular fractions following differential centrifugation of E18.5 *Kif21a*$^{+/+}$ (WT/WT) and *Kif21a*$^{KI/KI}$ (KI/KI) brain tissue lysates, and a graph quantifying the relative amount of Kif21a in each fraction. There were no significant differences in the relative amount of Kif21a in each fraction between WT and mutant mice (n=3). Mean ± SEM. ns=not significant. **(I)** Representative western blot and quantification of the relative amount of Kif21a in P4 and S4 fractions following differential centrifugation. *Kif21a*$^{KI/KI}$ brain lysates had a significantly higher relative amount of Kif21a in the P4 fraction and lower relative amount of Kif21a in the S4 fraction compared to WT brain lysates (n=3). Mean ± SEM. *p<0.05.

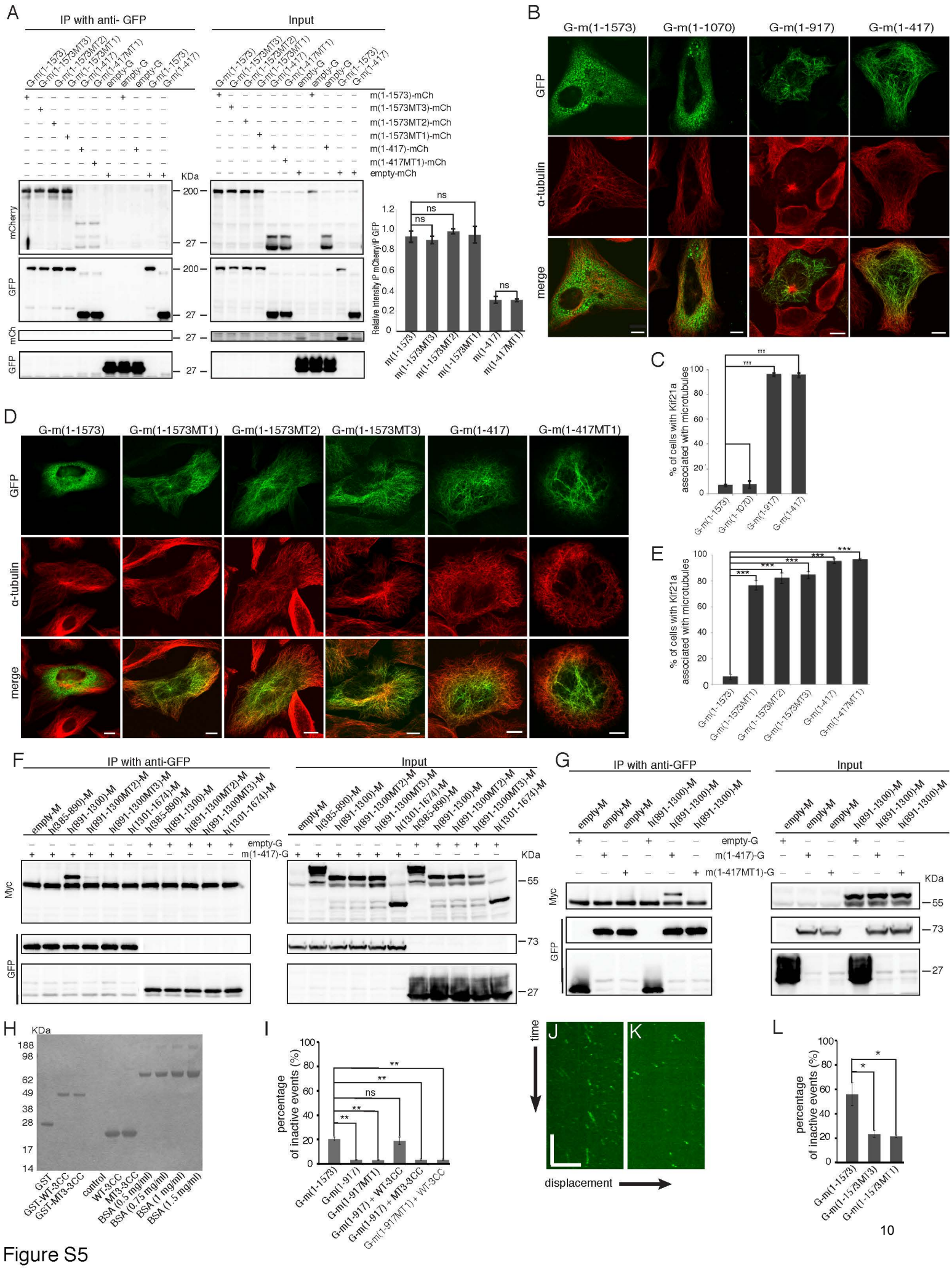
A
IP with anti- GFP
Input
G-m(1-1573)
G-m(1-1573MT3)
G-m(1-1573MT2)
G-m(1-1573MT1)
G-m(1-417)
G-m(1-417MT1)
empty-G
m(1-1573)-mCh
m(1-1573MT3)-mCh
m(1-1573MT2)-mCh
m(1-1573MT1)-mCh
m(1-417)-mCh
m(1-417MT1)-mCh
empty-mCh
KDa
200
27
mCherry
GFP
mCh
Relative intensity IP mCherry/IP GFP
ns
B
G-m(1-1573)
G-m(1-1070)
G-m(1-917)
G-m(1-417)
GFP
α-tubulin
merge
C
% of cells with Klf21a associated with microtubules
***
G-m(1-1573)
G-m(1-1070)
G-m(1-917)
G-m(1-417)
D
G-m(1-1573)
G-m(1-1573MT1)
G-m(1-1573MT2)
G-m(1-1573MT3)
G-m(1-417)
G-m(1-417MT1)
GFP
α-tubulin
merge
E
% of cells with Klf21a associated with microtubules
***
G-m(1-1573)
G-m(1-1573MT1)
G-m(1-1573MT2)
G-m(1-1573MT3)
G-m(1-417)
G-m(1-417MT1)
F
IP with anti-GFP
Input
empty-M
h(385-890)-M
h(891-1300)-M
h(891-1300MT2)-M
h(891-1300MT3)-M
h(1301-1674)-M
empty-G
m(1-417)-G
KDa
55
73
27
Myc
GFP
G
IP with anti-GFP
Input
empty-M
h(891-1300)-M
empty-G
m(1-417)-G
m(1-417MT1)-G
KDa
55
73
27
Myc
GFP
H
KDa
188
98
62
49
38
28
17
14
GST
GST-WT-3CC
GST-MT3-3CC
control
WT-3CC
MT3-3CC
BSA (0.5 mg/ml)
BSA (0.75 mg/ml)
BSA (1 mg/ml)
BSA (1.5 mg/ml)
I
percentage of inactive events (%)
**
ns
G-m(1-1573)
G-m(1-917)
G-m(1-917MT1)
G-m(1-917) + WT-3CC
G-m(1-917) + MT3-3CC
G-m(1-917MT1) + WT-3CC
J
K
time
displacement
L
percentage of inactive events (%)
*
G-m(1-1573)
G-m(1-1573MT3)
G-m(1-1573MT1)

Figure S5

Figure S5: CFEOM1 mutations enhance Kif21a-microtubule interactions in cells through attenuated interaction of the motor and 3rd coiled-coil domains. Related to Figure 6 and Supplemental Movies S3-S9.

(A) Representative western blot (n=3) of co-immunoprecipitation of over-expressed mouse mCherry-fused FL WT, MT1, MT2, or MT3 Kif21a by anti-GFP antibody in HEK293 cells. Quantification of the relative levels of co-precipitated mCherry-fused FL Kif21a in (A) revealed no significant differences between WT and mutant dimerization. Notably, the truncated stalk (1-417) with or without MT1 did not dimerize as efficiently as the FL constructs. Mean ± SEM, ns = not significant. Constructs and construct abbreviations are per Figure 5P. **(B)** Representative immunofluorescent images of HeLa cells stained with anti-α-tubulin antibody after extraction of soluble fractions reveal that over-expressed mouse GFP-fused FL (G-m(1-1573)) and WD40-truncated (G-m(1-1070)) Kif21a (green) appeared as puncta and not associated with microtubules (red), whereas truncation prior to 3rd coiled-coil domain (G-m(1-917)) or stalk domain (G-m(1-417)) resulted in Kif21a association with microtubules. Scale bars 10 μm. **(C)** Quantification of percentage of cells in (B) with microtubule-associated GFP-fused protein from 50 transfection-positive cells for each condition (n=3). Mean ± SEM. *** $p<0.001$, ns=not significant. **(D)** Representative immunofluorescent images stained with anti-α-tubulin antibody (n=3) show that mouse GFP-fused mutant (MT1, MT2, MT3) FL Kif21a and WT or mutant (MT1) stalk-truncated Kif21a (green) overexpressed in HeLa cells were associated with microtubules (red) after extraction of soluble fraction, while WT FL Kif21a (green) appeared as puncta and not associated with microtubules (red). Scale bars 10 μm. **(E)** Quantification shows percentage of cells in (D) with microtubule-associated GFP-fused protein from 50 transfection-positive cells for each condition (n=3). FL mutant Kif21a and stalk-truncated WT and mutant Kif21a had significantly increased microtubule association compared to FL WT Kif21a. Mean ± SEM. *$p<0.05$, **$p<0.01$, ***$p<0.001$, ns=not significant. Constructs and construct abbreviations are per Figure 5P. **(F and G)** Representative western blots (n=3 for (F) and n = 3 for (G)) showing that over-expressed Myc-tagged 3rd coiled-coil domain (h(891-1300)-M) specifically co-immunoprecipitated with GFP-fused motor (G-m(1-417)) domain from HEK293 cell lysates by anti-GFP antibody, and both (F) the 3rd coiled-coil MT2 and MT3 substitutions and (G) the motor domain MT1 substitution disrupted this co-immunoprecipitation**. (H)** SDS-PAGE and coomassie-blue staining of purified mouse WT and mutant 3rd coiled-coil domains (WT-3CC and MT3-3CC). **(I)** Quantification of the percentage of landing events that resulted in inactive 'dead' motors in Figure 6 (E-J), **(J and K)** Representative kymographs showing the displacement on a microtubule over 5 minutes in BRB80 motility buffer of mouse GFP-fused mutant FL Kif21a {G-m(1-1573MT3)} (J) and {G-m(1-1573MT1)} (K). **(L)** Quantification of the percentage of landing events that resulted in inactive 'dead' motors in Figure 6 (L-N). For each construct, data were acquired from two independent experiments, and from three time-lapsed images for each experiment. Mean ± SEM. *$p<0.05$, **$p<0.01$, ns=not significant. Constructs and construct abbreviations are per Figure 5P.

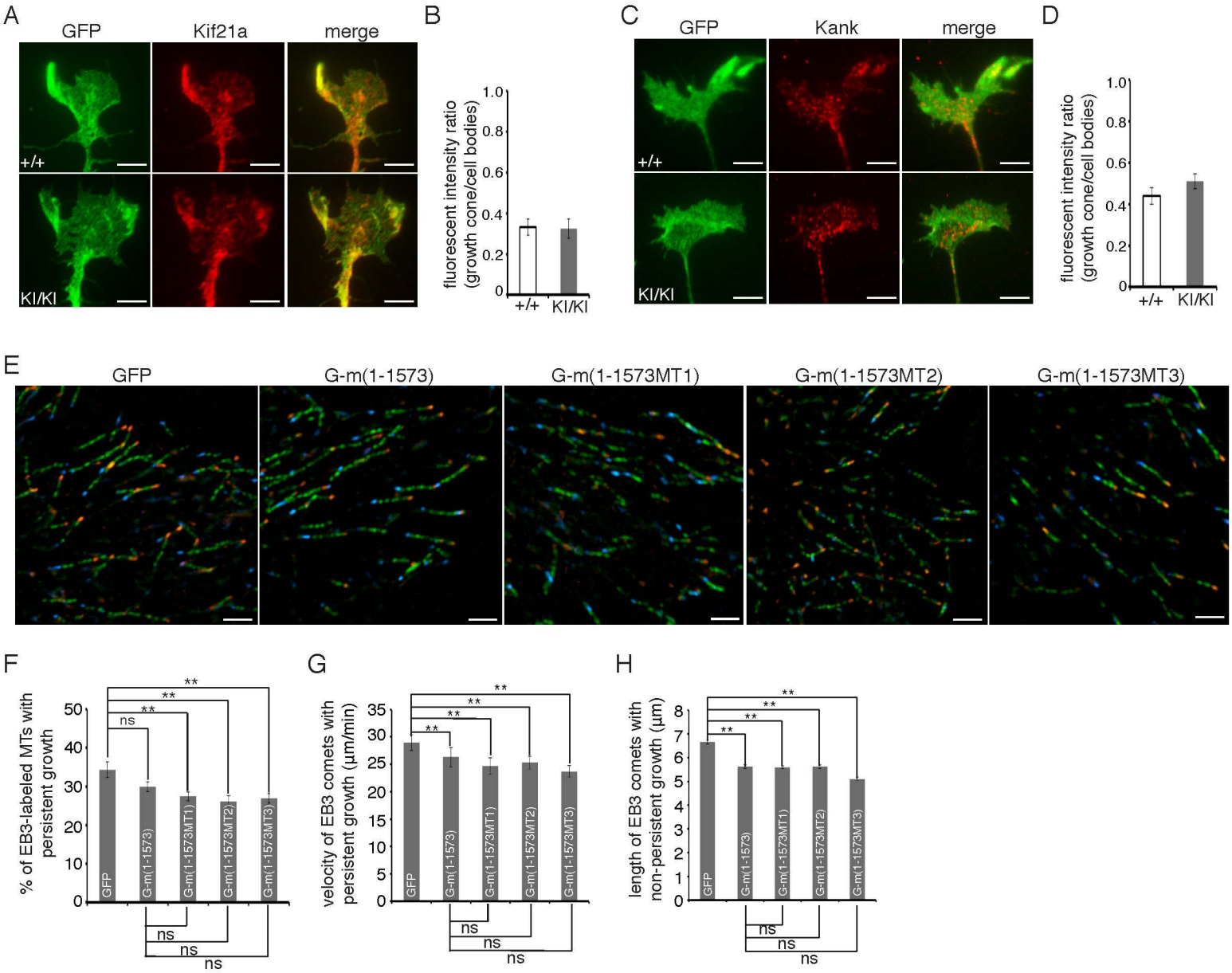
A
GFP
Kif21a
merge
+/+
KI/KI
B
fluorescent intensity ratio (growth cone/cell bodies)
1.0
0.8
0.6
0.4
0.2
0
+/+
KI/KI
C
GFP
Kank
merge
+/+
KI/KI
D
fluorescent intensity ratio (growth cone/cell bodies)
1.0
0.8
0.6
0.4
0.2
0
+/+
KI/KI
E
GFP
G-m(1-1573)
G-m(1-1573MT1)
G-m(1-1573MT2)
G-m(1-1573MT3)
F
% of EB3-labeled MTs with persistent growth
50
40
30
20
10
0
**
**
**
ns
GFP
G-m(1-1573)
G-m(1-1573MT1)
G-m(1-1573MT2)
G-m(1-1573MT3)
ns
ns
ns
G
velocity of EB3 comets with persistent growth (µm/min)
35
30
25
20
15
10
5
0
**
**
**
**
GFP
G-m(1-1573)
G-m(1-1573MT1)
G-m(1-1573MT2)
G-m(1-1573MT3)
ns
ns
ns
H
length of EB3 comets with non-persistent growth (µm)
8
7
6
5
4
3
2
1
0
**
**
**
**
GFP
G-m(1-1573)
G-m(1-1573MT1)
G-m(1-1573MT2)
G-m(1-1573MT3)
ns
ns
ns

Figure S6

Figure S6: Oculomotor axon growth cones in *Kif21a*$^{KI/KI}$ explant cultures shows normal accumulation of Kif21a and Kank. CFEOM1 mutations do not alter microtubule growth and dynamics in COS7 cells. Related to Figure 7.

(A-D) Representative immunofluorescent images are shown of *Isl*^{MN}*:GFP Kif21a*$^{KI/KI}$ and *Kif21a*$^{+/+}$ oculomotor growth cones immunostained with anti-Kif21a (A), and Kank (C) antibodies. Quantification revealed no significant differences between the ratio of the fluorescence intensity in the oculomotor growth cone versus cell body of Kif21a in WT versus *Kif21a*$^{KI/KI}$ mice (B) (n=3, 3), and Kank (D) (n=5, 4). Mean ± SEM. Scale bars 5 μm. **(E)** Representative images of maximum projections of EB3-mCherry in 10 frames (interval=2s) of a 20 second time-lapse movies of COS7 cells co-transfected with GFP control or GFP-fused FL WT and mutant Kif21a constructs. For each EB3-mCherry tracking event, the first frame is shown in blue, the last frame in red, and the intermediary frames in green. Scale bars 10 μm. **(F-H)** Quantification from (E) of n=12, 10, 17, 10, 19 cells and 1218, 1114, 1703, 1081, 1526 EB3-labelled microtubule plus-ends. (F) Percentage and (G) velocity of persistent microtubule growth; (H) length of non-persistent microtubule growth. Mean ± SEM. **p<0.01, ns=not significant. Constructs are per Figure 5P.

2. Supplemental Movie Legends

Movie S1: Three-dimensional rotating movie of distal oculomotor (III), trochlear (IV), and abducens (VI) nerves in an E14.5 *Kif21a*$^{+/+}$*;Isl*^{MN}*:GFP* embryo obtained using 2-photon microscopy. Note the normal trajectories of the three nerves, including the superior division of the oculomotor nerve as it branches away from the inferior division. Related to Figures 2 and S2.

Movie S2: Three-dimensional rotating movie of the distal oculomotor (III), trochlear (IV), and abducens (VI) nerves in an E14.5 heterozygous *Kif21a*$^{+/KI}$*;Isl*^{MN}*:GFP* littermate of the WT embryo in Movie S10. Note that while the three nerves appear to have normal trajectories, the oculomotor superior division (superior III) is remarkably thinner than in the WT orbit (Movie S10). Globe: position of eyeball relative to the nerves. Related to Figures 2 and S2.

Movie S3: Single molecule imaging of mouse GFP-fused WT FL (G-m(1-1573)) Kif21a proteins (green) moving on Cy5-labeled microtubules (red) in BRB80 motility buffer. Movie duration is 5 min. Note that only rare WT Kif21a motors are bound to microtubules and move processively, while a large number of motors remain in solution. Related to Figures 6 and S5.

Movie S4: Single molecule imaging of mouse GFP-fused WT Kif21a protein truncated prior to the 3rd coiled-coil domain (G-m(1-917)) (green) moving on Cy5-labeled microtubules (red) in BRB80 motility buffer. Movie duration is 5 min. Compared to WT full length Kif21a, many more WT truncated Kif21a motors are bound to microtubules and move processively. Related to Figures 6 and S5.

Movie S5: Single molecule imaging of mouse GFP-fused mutant Kif21a truncated prior to the 3rd coiled-coil domain (G-m(1-917MT1)) (green) moving on Cy5-labeled microtubules (red) in BRB80 motility buffer. Movie duration is 5 min. A similar number of mutant truncated Kif21a motors bind to microtubules and move processively compared to WT truncated motors (Movie S2). Related to Figures 6 and S5.

Movie S6: Single molecule imaging of mouse GFP-fused WT Kif21a truncated prior to the 3rd coiled-coil domain (G-m(1-917)) (green) incubated with 50 μM purified WT-3rd coiled-coil domain moving on Cy5-labeled microtubules (red) in BRB80 motility buffer. Movie duration is 5 min. Compared to WT Kif21a truncated prior to 3rd coiled-coil domain (G-m(1-917)) alone (Movie S1), many fewer Kif21a motors are bound to microtubules and move processively. Related to Figures 6 and S5.

Movie S7: Single molecule imaging of mouse GFP-fused WT Kif21a truncated prior to the 3rd coiled-coil domain (G-m(1-917)) (green) incubated with 50 μM purified mutant (MT3) 3rd coiled-coil domain moving on Cy5-labeled microtubules (red) in BRB80 motility buffer. Movie duration is 5 min. Compared to incubation with 50 μM purified WT 3rd coiled-coil domain (Movie S4), many WT truncated Kif21a motors are now bound to microtubules and move processively. Related to Figure 6 and S5.

Movie S8: Single molecule imaging of mouse GFP-fused mutant Kif21a truncated prior to 3rd coiled-coil domain (G-m(1-917MT1)) (green) incubated with 50 μM purified WT 3rd coiled-coil domain moving on Cy5-labeled microtubules (red) in BRB80 motility buffer. Movie duration is 5 min. Compared to WT truncated Kif21a (G-m(1-917)) incubated with 50 μM purified WT 3rd

coiled-coil domain (Movie S4), many more mutant truncated Kif21a motors are bound to microtubules and move processively. Related to Figures 6 and S5.

Movie S9: Single molecule imaging of mouse GFP-fused **(A)** WT FL (G-m(1-1573)) Kif21a, **(B)** mutant FL (G-m(1-1573MT3)) Kif21a, and **(C)** mutant FL (G-m(1-1573MT1)) Kif21a (green) moving on Cy5-labeled microtubules (red) in BRB30 motility buffer. Each movie duration is 10 min. Note in (A) that only a small number of WT Kif21a motors are bound to microtubules and move processively, while a large number of motors remain in solution. In comparison, in (B) and (C), many more mutant Kif21a motors are bound to microtubules and move processively. Related to Figures 6 and S5.